Corrosion Science 173 (2020) 108828

Contents lists available at ScienceDirect

Corrosion Science

journal homepage: www.elsevier.com/locate/corsci

The oxidation effect on the cracking behavior of a Co-based alloy under thermal shocks

Junxia Wen[a,b,c,d], Rui Cao[a,b,*], Hongyan Che[e], Hao Dong[e], Haiyan Zhang[a,b], Yingjie Yan[a,b], Yanfei Gao[c,**], Peter K Liaw[c,**]

[a] State Key Laboratory of Advanced Processing and Recycling of Non-ferrous Metal, Lanzhou University of Technology, Lanzhou, 730050, Gansu, China
[b] School of Materials Science and Engineering, Lanzhou University of Technology, Lanzhou, 730050, Gansu, China
[c] Department of Materials Science and Engineering, The University of Tennessee, Knoxville, TN, 37996, USA
[d] School of Mechanical and Electrical Engineering, Liuzhou Vocational & Technical College, Liuzhou 545006, Guangxi, China
[e] Advanced Technology & Materials Limited Company, China Iron & Steel Research Institute Group, Beijing, 100081, China

ARTICLE INFO

Keywords:
Co-based alloy
Thermal shock
Oxidation
Crack
Thermal fatigue

ABSTRACT

Oxidation and cracking behavior during thermal-shock experiments of a new Co-based alloy were analyzed in the present work. Comparing to the static conditions, the oxidation behavior during thermal shocks is stress-assisted and crack-accelerated. Cracks during the thermal shocks were initiated from the sample surfaces and their growth are driven by various stresses, including those induced by volume change, mismatch of coefficients of thermal expansion (CTEs), and temperature gradient between the matrix and the internal oxides. It is found that the crack propagation correlates to these stresses in the classic Paris' law.

1. Introduction

The Co-based alloy has a good combination of high-temperature toughness, wear resistance, and excellent oxidation resistance for long-term exposure [1–3]. It is extensively applied in aerospace, chemical, petrochemical industries, and power plants [4–6]. Components working at high temperatures are expected to perform at elevated operating temperatures to produce high efficiency [7]. At the same time, high operating temperatures mean that drastic temperature variations can be produced during the startup and shutdown. In other applications, for example, in the cutting field, the repeated thermal variations are induced during the cutting and cooling of the cutting tools. Temperature distributions on the components in the process of heating and cooling are not uniform, which can produce enormous thermal stresses [8]. Repeated compressive-tensile stress cycles associated with the repeated abrupt temperature variations cause drastic degradation of materials [9–12]. Mechanical fatigue caused by the thermal stress and oxidation at elevated temperatures leads to the degradation of the material. The investigation of the oxidation and cracking behavior under thermal cycles is thus becoming an important issue to superalloys in high-temperature fatigue.

Oxides generated in the cyclic oxidation of the Co-based alloy are also different from that in the static oxidation. The cyclic oxidation behavior of the Co-based alloy has been well investigated by Barrett and Lowel [13]. They conducted a series of cyclic oxidation experiments of Co-Cr-Al/Ni alloys in air at 1100 °C and 1200 °C. The results indicated that if the Al contents in both systems are high enough, a protective oxide layer with α-$A1_2O_3$ oxides can be generated. However, in the long time run, when the oxide layers eventually start to fail, the dominant CoO is formed in the Co-Cr-Al system and NiO in the Ni-Cr-Al system.

Fracture mechanism is the main concern in the research of thermal fatigue. Fatigue life, fatigue resistance, and residual mechanical properties of the alloy are closely related to the operating temperatures [8,14–16]. The occurrence of oxidation at high temperatures has a significant influence on these factors [17,18]. The detrimental influences of oxidation on the degradation of materials are possibly attributed to oxidation-induced, oxidation-assisted or oxidation-accelerated internal cracks initiated on the surface. The mechanism of the internal cracks have been investigated in the Co–Cr alloy [14,19] and in the Ni-base superalloy [20,21]. Cracks and final failures produced during high-temperature fatigue are directly related to the preferential oxidation at grain boundaries, because the diffusion coefficients of some elements (Cr or Al, most time) at the grain boundaries is higher than

* Corresponding author at: State Key Laboratory of Advanced Processing and Recycling of Non-ferrous Metal, School of Materials Science and Engineering, Lanzhou University of Technology, Lanzhou, 730050, Gansu, China.
** Corresponding authors at: Department of Materials Science and Engineering, The University of Tennessee, Knoxville, TN, 37996, USA.
E-mail addresses: caorui@lut.edu.cn (R. Cao), ygao7@utk.edu (Y. Gao), pliaw@utk.edu (P.K. Liaw).

https://doi.org/10.1016/j.corsci.2020.108828
Received 22 December 2019; Received in revised form 7 June 2020; Accepted 20 June 2020
Available online 26 June 2020
0010-938X/

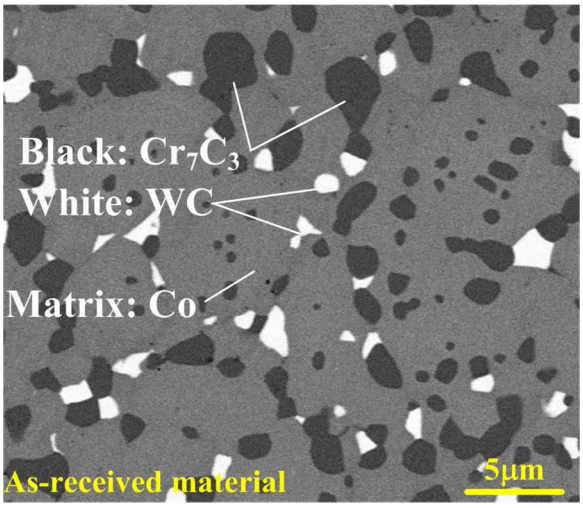

Fig. 1. Microstructure of the as-received Co-based alloy.

that in the matrix [22,23]. The diffusion of elements can be accelerated by high temperatures and tensile stresses [24,25], which leads to serious oxidation.

Thermal shock is an issue that involves the cyclic oxidation and cyclic thermal stress. However, most literature works only pay attention to the oxidation in the cyclic oxidation and fatigue during cyclic loading. Less attention is concentrated on the cracking behavior during cyclic oxidation and the oxidation during cyclic loading.

In the present work, a new kind of Co-based alloy was manufactured by the Hot Isostatic Pressing (HIP) sintering technology. This new Co-based alloy has a much more homogeneous microstructure and includes fine carbides particles. A series of thermal-shock tests had been conducted to investigate the oxidation behavior and the cracking behavior of this new Co-based alloy [6,26,27]. X-Ray Diffraction (XRD), Scanning Electron Microscopy (SEM), and Energy Dispersion Spectrum (EDS) were adopted to analyze the contents of oxides, microstructures, crack morphologies, and element-distribution maps. A hypothesis was proposed to explain the features of oxidation and cracking behaviors under thermal-shock conditions.

2. Materials and experimental procedures

The main composition of this new Co-based alloy is Co-29Cr-2.3C-3W (atomic percent, at %). The original powder supplied to the HIP process was produced by the inert-gas-metal atomization (IGMA) technique. IGMA is used to produce spherical metal powders [28]. These powder particles range from 2 to 20 μm in diameters. The Co-based alloy subjected to thermal-shock experiments was machined with geometry dimensions of 32 mm × 3 mm × 4 mm. Its microstructure presented in Fig. 1 demonstrates that this Co-based alloy consists of the WC particles with the mean diameter of 0.6 μm, Cr_7C_3 particles with the mean diameter of 0.9 μm, and Co matrix with the mean diameter of 7 μm. The areal fraction of WC particles and Cr_7C_3 particles is about 6% and about 22%, respectively. Samples subjected to thermal shocks were machined by the electric-discharge machine. All surfaces were ground and polished with the metallographic sandpaper, ensuring that the surface roughness is below 0.8 μm.

The heating procedures during thermal shocks were carried in the air in a box furnace. Samples were first placed into the furnace that has

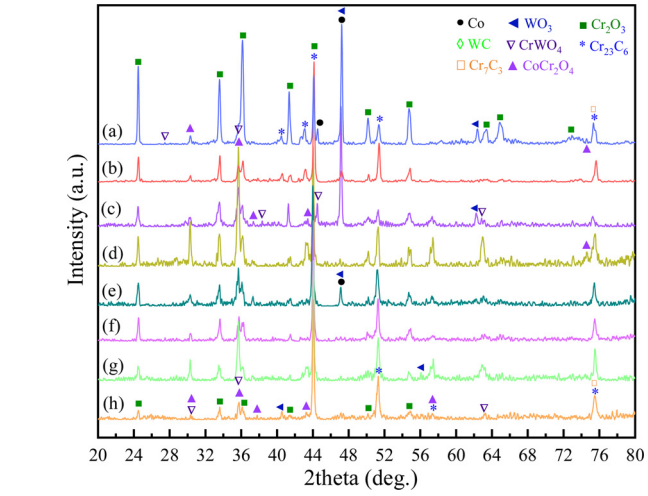

Fig. 3. XRD patterns of the surface oxides. Static oxidation in air at 800 °C for (a) 100 h, and (b) 1 h. Thermal shock at temperatures of 800 °C - RT for (c) 90 cycles, (d) 75 cycles, (e) 60 cycles, (f) 45 cycles, (e) 30 cycles, and (h) 15 cycles.

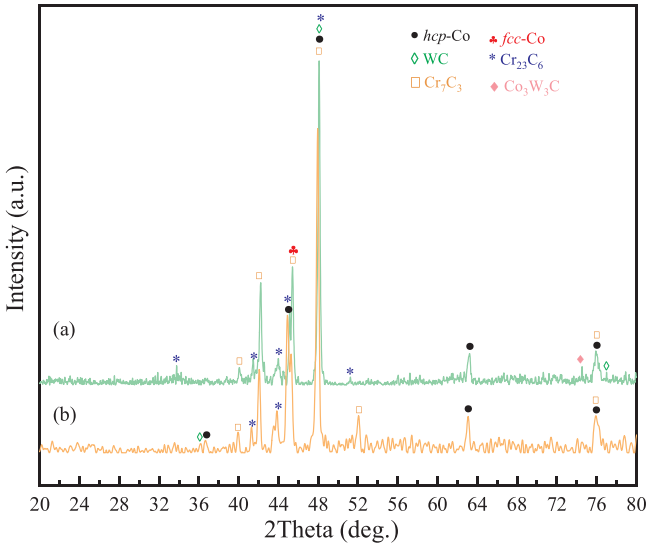

Fig. 4. XRD patterns of the substrate, (a) after 150 thermal-shock cycles at temperatures of 800 °C - RT, and (b) in the as-received material.

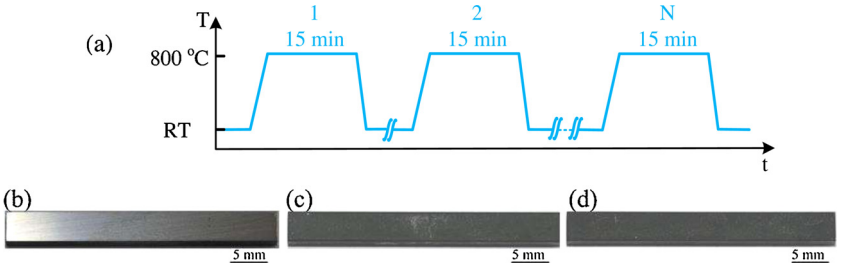

Fig. 2. Thermal-shock procedure and samples. (a) Schematic diagram of the thermal-shock procedure at temperatures of 800 °C - RT, and samples (b) before thermal shocks and after (c) 60, (d) 75 thermal-shock cycles.

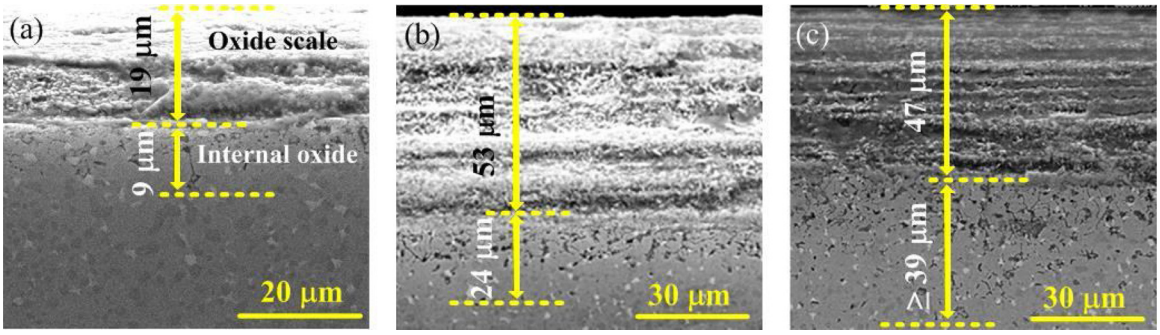

Fig. 5. Comparison of the oxide scales and the internal oxide zones after various thermal shocks at temperatures of 800 ℃ - RT. (a) 30 cycles, (b) 60 cycles, and (c) 75 cycles.

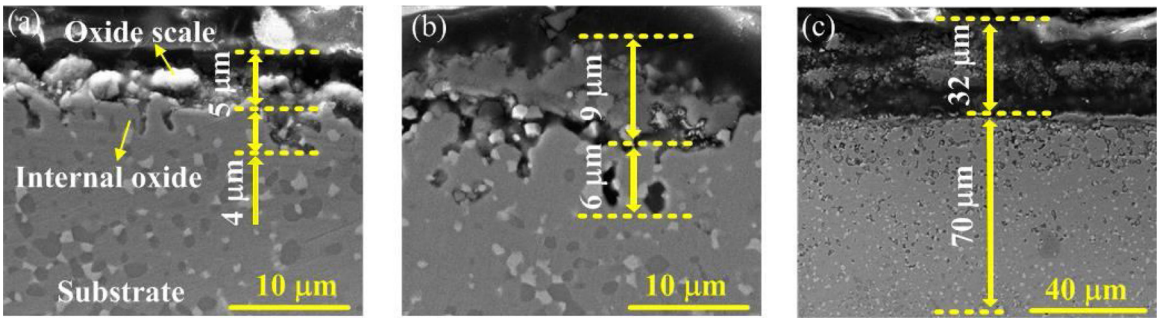

Fig. 6. Comparison of the oxide scales and the internal oxide zones after various oxidation times in air at 800 ℃. (a) 100 h, (b) 150 h, and (c) 200 h.

been heated up to 800 ℃ and then exposed in the furnace for 15 min, and finally quenched in the water at room temperature. The temperature variation in the thermal-shock procedure is sketched in Fig. 2. The cycles of thermal shocks were repeated as 15, 30, 45, 60, 75, and 90, respectively. More details about this material and the thermal shock procedures could refer to Refs [6,27]. The difference between thermal shocks and the cyclic oxidation elaborated in Refs. [13,29] is the cooling medium and the cooling rate. The cyclic oxidation usually cools in air and has a relatively slow cooling rate.

To understand the oxidation mechanism during thermal shocks, static oxidation is comparably conducted. Static oxidation was performed in air in a box furnace at 800 ℃ and the oxidation time was 1 h, 100 h, 150 h, and 200 h, respectively.

One specimen in every group was randomly chosen to observe the internal oxidation and cracks. The cross-section specimens were prepared following the standard metallography techniques. The thickness of the internal oxidation and the length of cracks were observed by Scanning electron microscopy (SEM, JSM-7001 F/JEOL). The surface oxides on the thermal-shock specimens were identified by the XRD technique using an X' Pert PRO X-ray diffractometer. SEM with backscattered electron (BSE) imaging was adopted to observe the distribution of the elements around the cracks generated during thermal shocks.

3. Results

3.1. XRD analysis of the oxides and the substrate

Fig. 3 compares the XRD patterns of the surface oxides after static oxidation with that after thermal shocks. The oxides formed during thermal shocks are similar to those during static oxidation. Peaks of Cr_2O_3, WO_3, $CrWO_4$, $CoCr_2O_4$, and $Cr_{23}C_6$, as shown in Figs. 3(a)-(h), are detected both in the static oxidation and in the thermal-shock oxidation. A dominant amount of Cr_2O_3 peaks and minimum amounts of $CrWO_4$ and Co_2CrO_4 peaks are detected in the oxides of static oxidation at 800 ℃, presented in Figs. 3(a) and (b). The oxides generated by thermal shocks mainly consist of Cr_2O_3 and $CoCr_2O_4$, and a small amount of WO_3 and $CrWO_4$. Obvious peaks of $Cr_{23}C_6$ are detected on the surfaces both after static oxidation and thermal shocks. The formation of $Cr_{23}C_6$ is one of the decarburization steps in the oxidation of Cr_7C_3, where carbon is removed as gaseous CO, and Cr is oxidized into Cr_2O_3 [30].

It is found that the phases in the material subjected to thermal shocks are a little different from that in the as-received material, as presented in Fig. 4. From Fig. 4(b), the as-received material is composed of the Co, Cr_7C_3, $Cr_{23}C_6$, and WC phases. After 150 thermal shocks at temperatures of 800 ℃ - RT, a little peak of Co_3W_3C is detected in Fig. 4(a), and the minor change can be found in the peaks of face-centered-cubic (*fcc)*-Co and Cr_7C_3. A new Co_3W_3C phase is formed in the process of thermal shocks, which has been discussed in Ref. [27]. According to their Gibbs formation energy [30], the $Cr_{23}C_6$ is much more stable than Cr_7C_3 at 800 ℃. And the in-situ transformation of $M_7C_3 \rightarrow M_{23}C_6$ has been directly observed in the aging treatment of a single-crystal cobalt-base superalloy at 1100 ℃ by Gui. et al. [31]. Based on the above analysis, the amount of $Cr_{23}C_6$ should increase while the amount of Cr_7C_3 should decrease during the thermal-shock process. For the present Co-based alloy, the transformation temperatures range of hexagonal close-packed (*hcp)*-Co → *fcc*-Co is 735 ℃ ~ 834 ℃ according to the calculation of the phases diagram by the software of JmatPro. This feature, corresponds to the experimental result of another Co-based ally [32], whose transformation temperatures range of *hcp*-Co → *fcc*-Co is 740 ℃ ~ 950 ℃. This trend means that the content of *fcc*-Co phase increases while the content of *hcp*-Co phase decreases with the increase of thermal shocks at temperatures of 800 ℃ - RT.

3.2. Oxidation during the thermal shocks and static oxidation at 800 ℃

To understand the degree of oxidation during thermal shocks, the cross-section images of the oxidized samples after various thermal-shock cycles and various times of static oxidation are presented in Figs. 5 and 6, respectively. The measured thicknesses of the oxide scales

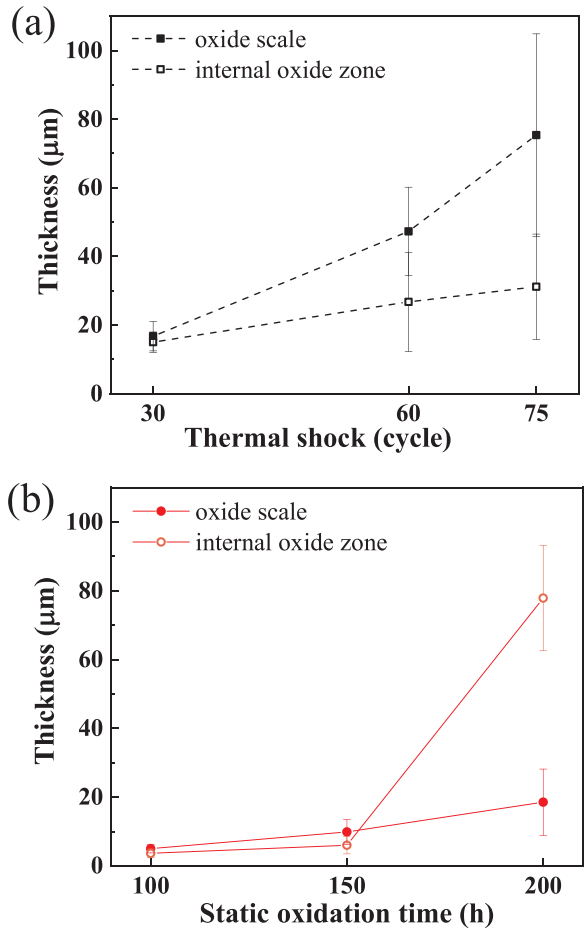

Fig. 7. Comparison of the thicknesses of the oxide scales and internal oxide zones. (a) Produced during thermal shocks at temperatures of 800 ℃ - RT. (b) Produced at static oxidation in air at 800 ℃.

and the internal oxide zones are compared in Fig. 7.

Fig. 5 presents the features and thickness of the oxide scale, internal oxide zone, and the substrate in specimens after various thermal-shock cycles at temperatures of 800 ℃ - RT. The microstructures of the substrate shown in Figs. 5(a) - (c) are similar to that of the as-received material presented in Fig. 1. A distinguishable internal oxidation zone beneath a quite thick oxide scale could be formed after several thermal-shock cycles. After 30 thermal-shock cycles, exhibited in Fig. 5(a), the thickness of the internal oxide and the oxide scale is about 9 μm and 19 μm, respectively. After 60 thermal-shock cycles, shown in Fig. 5(b), the thickness of the internal oxide zone and the oxide scale increases to about 24 μm and 53 μm, respectively. After 75 thermal-shock cycles, shown in Fig. 5(c), the thickness of the internal oxide zone and the oxide scale reaches about 39 μm and 47 μm, respectively. As shown in Fig. 7(a), the thickness of the oxide scales and the internal oxide zones are approximately increased with the increased thermal-shock cycles. However, the thicknesses of the oxide scales and the internal oxide zones are somewhat scattered because of the peeling off ofoxide scales during the process of thermal shocks.

Fig. 6 shows the cross-section image of the samples after various times of static oxidation at 800 ℃. As presented in Figs. 6(a) and (b), the thicknesses of the oxide scales and the internal oxide zones formed in 100 h and 150 h are very thin, and only less than 10 μm. After oxidation in air for 200 h at 800 ℃, the thickness of the oxide scale and the internal oxide zone increases to about 32 μm and 70 μm, respectively. As exihibited in Fig. 7(b), the thickness of the oxide scales and the internal oxide zones have a minor increase before 150 h. After static oxidation for 200 h, the internal oxidation is catastrophic but the oxide scale is relatively thin. This trend indicates that the oxide scale is seriously peeling off after static oxidation at 800 ℃ for 200 h.

3.3. Cracks during the thermal shocks

Fig. 8 shows the longest cracks on the observed cross sections of samples after various thermal-shock cycles. No apparent cracks can be produced on the specimen within 15 thermal-shock cycles. After 30 thermal-shock cycles, cracks were observed in specimens, as exhibited in Fig. 8. The crack length gradually increases with the increase of thermal-shock cycles.

3.4. *Elemental* distribution around the crack during thermal shocks

Fig. 9(a) shows the SEM map of a whole crack with an oxide scale on it. EDS-maps shown in Figs. 9(b), (c), and (d) present the elemental distributions at the locations of the beginning of the crack, the mid-crack, and the crack tip, which is corresponded to the region in Fig. 9(a) marked by yellow square frame I, II, and III, respectively. Elemental maps in Figs. 9(b), (c), and (d) indicate that Cr and O elements are all rich in the oxide scale, the internal oxide, and the crack. The morphology of the cracks in Fig. 9 is similar to that observed by Tunthawiroon et al. [14] in high-temperature isothermal fatigue experiments of the Co-based, and Valsan et al. [19] in elevated-temperature isothermal fatigue experiments of the PE-16 superalloys.

As shown in Fig. 5, internal oxides are produced under the oxide scales and penetrate the substrate. The internal oxides with the pocket-like feature are generated around the Cr_7C_3 particles. In Fig. 9 (a), the internal oxides is not only dispersed beneath the oxide scale but also around the cracks generated during the thermal shocks, which is also observed in Fig. 8. At the beginning of thermal shocks, the internal oxides are of pocket-like feature, and no obvious Cr-depletion zone can be found under the oxide scale because the Cr_7C_3 phases haven't been totally consumed. After more thermal-shock cycles, the internal oxides became dendritic, and distributed along the grain boundaries as a result of the short-circuit diffusion of O and Cr elements [22,23,33] at grain boundaries. And then the internal oxides become intergranular oxides. The thickness of the internal oxide zone increases with the increase of thermal-shock cycles. The oxidation rate is much faster than that in static oxidation due to the dendrite internal oxides and cracks.

The SEM-EDS elemental mapping of the crack tip in Fig. 9(d) demonstrates that Cr and O elements are rich in the crack tip. The Cr-rich internal oxide is less protective to prevent further oxidation in the thermal-shock process due to their porosity and poor coherence with the matrix. The content of oxygen in the crack is high enough for the Cr elements to be selectively oxidized in the crack. When oxygen diffuses into the crack, it reacts rapidly with the Cr elements and then forms dominant Cr-rich oxides.

4. Discussion

4.1. Paris' law and the cracking behavior during thermal shocks

The length of the longest cracks presented in Fig. 8 is drawn in Fig. 10. Only the longest crack length data on the observed cross sections of the specimens after various thermal-shock cycles were picked out because the length of the cracks is dispersive. The crack length increases with the increase of thermal-shock cycles, and the crack growth curve obeys Paris' law [34].

$$da/dN = C(\triangle K)^m \quad (1)$$

Where a is the crack length, N is the cycles of thermal shocks, and da/dN is the crack growth rate for one thermal-shock cycle. C and m are material constants, which are experimentally determined and depend on the environment [35]. $\triangle K$ is the stress intensity range and is

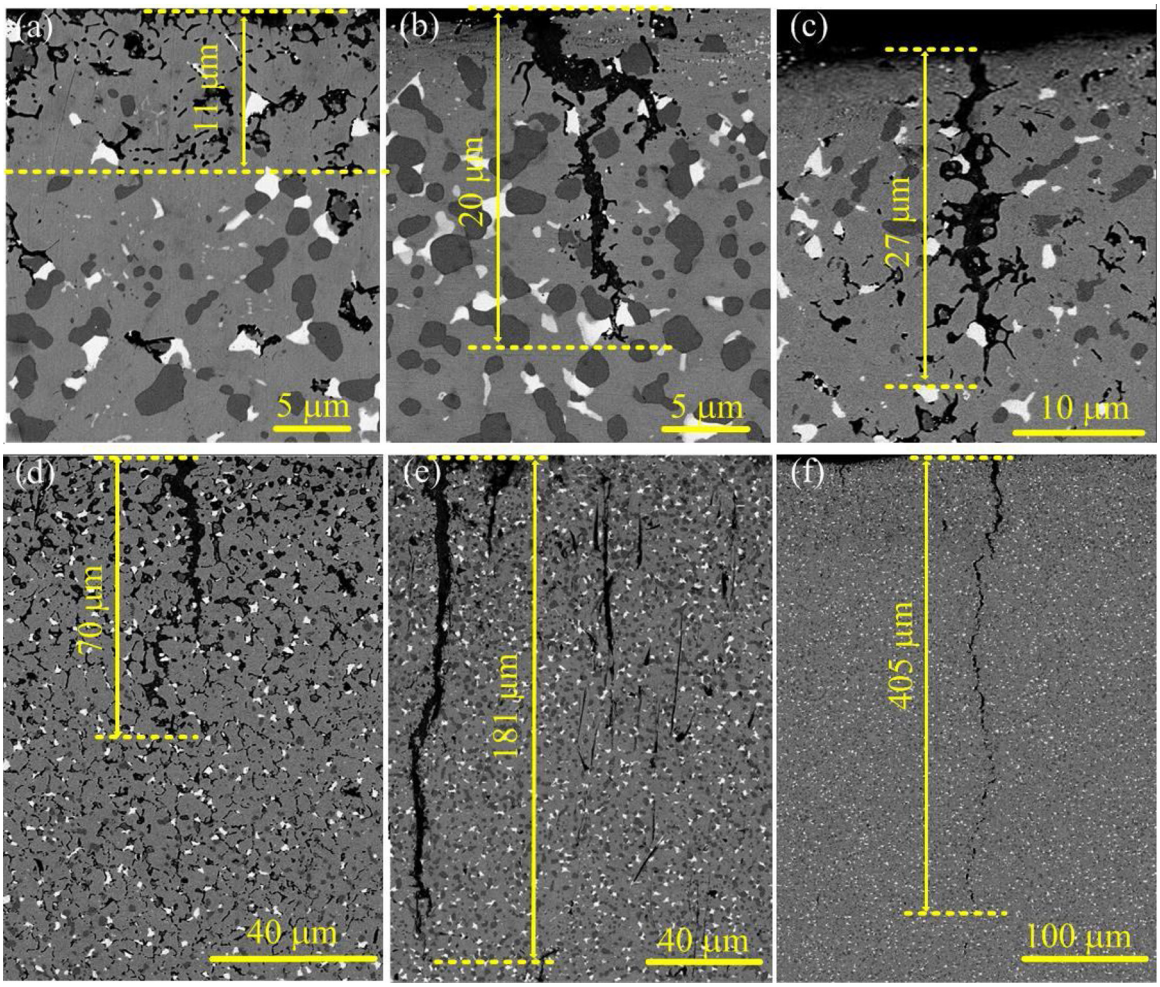

Fig. 8. The longest cracks in the observed specimens after various thermal-shock cycles at temperatures of 800 ℃ - RT. (a) 15 cycles, (b) 30 cycles, (c) 45 cycles, (d) 60 cycles, (e) 75 cycles, and (f) 90 cycles.

determined by the stress gradient and crack length [36].

$$\Delta K = Y\Delta\sigma\sqrt{a} \tag{2}$$

Y is a constant. The stress gradient is constant because the gradient of temperature is constant. The Paris' law could be modified into:

$$da/dN = A\sqrt{a}^{m} \tag{3}$$

A is a constant. We do the logarithm of both sides of Eq. (3). Eq. (3) can be written as:

$$Ln\left(\frac{da}{dN}\right) = LnA + mLn\sqrt{a} \tag{4}$$

Fig. 11 presents a linear fit between the values of $Ln\left(\frac{da}{dN}\right)$ versus the value of $Ln\sqrt{a}$. The value of m and A could be calculated from the slope and the intercept of the fitting line respectively. The fitted results in Fig. 11 can be expressed as Eq. (5).

$$da/dN = 0.0171\sqrt{a}^{2.296} \tag{5}$$

Eq. 5 illustrates that the crack growth rate of the thermal shocks at temperatures of 800℃- RT increases with the crack length of a. The crack growth rate exponentially increases with the increase of crack length.

4.2. Transient thermal stress at the moment of heating and cooling

Fig. 12 shows the schematic illustration of the transient thermal stress generated during the thermal-shock processes. At the beginning of heating, the temperature gradient is not uniform in the specimen. The surface of the specimen is heated up to 800℃ at the moment of putting into the furnace. It needs a certain time for the inside of the specimen to be heated up to 800℃. This time depends on the heat conductivity and the thickness of the specimen. During the heating moment, the surface and the inside of the specimen changes from states 1 into 2, as presented in Fig. 12(a). Because of the different temperatures, the inside and the surface of the specimens have different expansions. The surface of the specimen has great expansion and is subjected to a compressive stress. The inside of the specimen has a small expansion and is subjected to a tensile stress. The thermal stress generated in the moment of the cooling process is vice-versa, as presented in Fig. 12(b).

The crack growth rate is dominantly determined by the temperature gradient in the thermal-shock experiment, which could be calculated by:

$$\sigma = \frac{E}{1-\mu}\alpha\Delta T \tag{6}$$

where α is the coefficient of thermal expansion (CTE). μ is the Poisson's ratio, here is about 0.3. $\Delta T = T_{max} - RT = 780$ ℃. E is the elastic modulus. Here, two assumptions were suggested to calculate the thermal stress induced on the surface of the specimen. (i) There was no heat transient into the specimen but only the surface. (ii) E and α are constants. According to the thermophysical and mechanical parameters listed in Table 1, the extreme thermal stress calculated by Eq. (6) is 2.54 GPa.

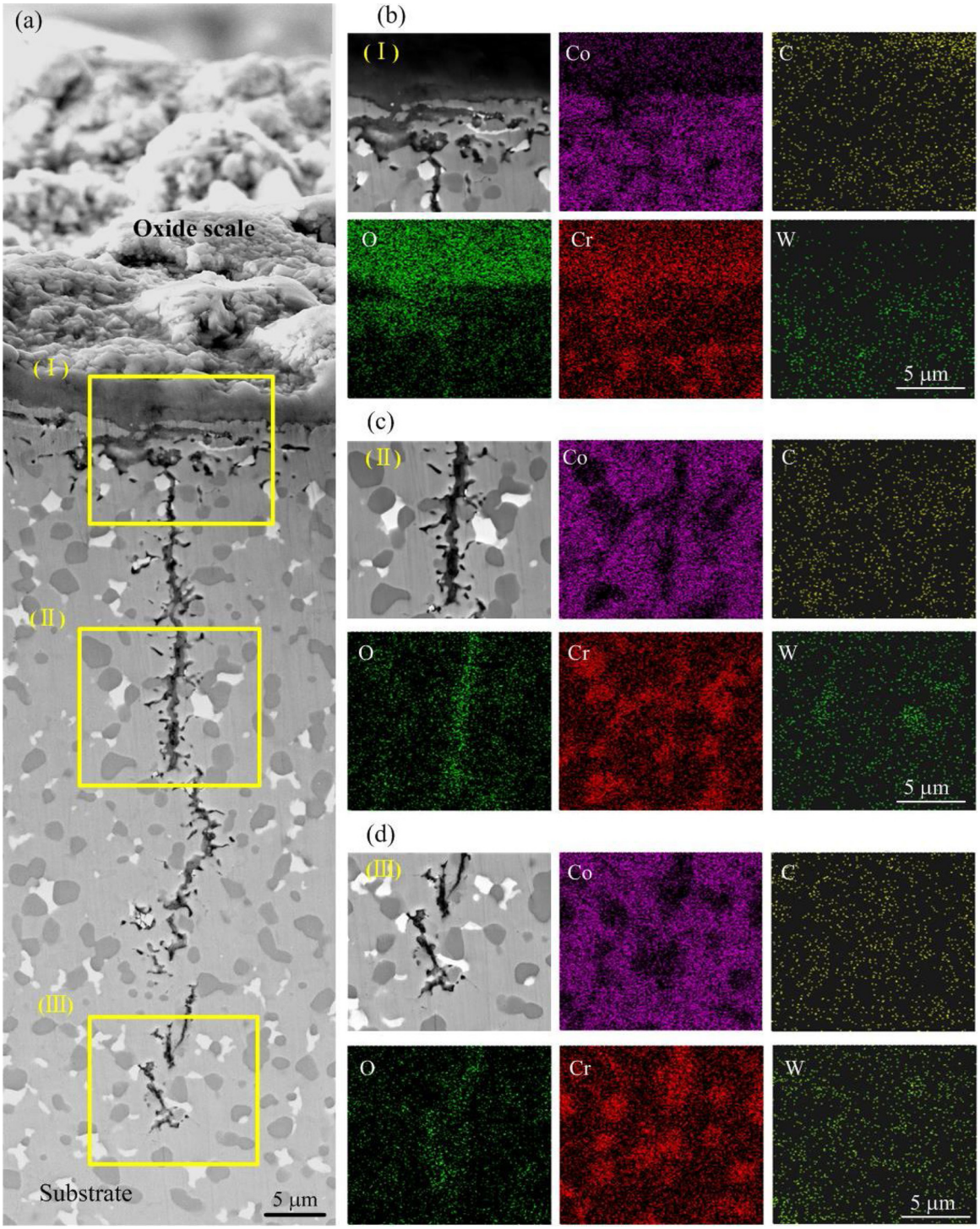

Fig. 9. SEM cross-section images and the elemental maps around one crack on the specimen after 75 thermal-shock cycles at temperatures of 800 ℃ - RT.

4.3. *Interactions* of oxidation and cracks during thermal shocks

Comparing to the static oxidation at the temperatures of 800 ℃, the oxidation during the thermal shocks is disastrous as a result of the internal oxides and the cracks. Several suggestions can be put forward to explain the stresses induced by oxidation during thermal shocks.

(i) Elements distribution maps in Fig. 9(d) indicate that there are a greater amount of oxide inclusions at the crack tip. Compression stress is expected around the crack tip due to the volume expansion of internal oxides. According to the calculation of strain induced by volume expansion of oxides in Ref. [42], the stress induced in the matrix could be calculated by Eq. (7):

$$\sigma_m = \frac{E_m}{1-\mu_m}\frac{(1-\sqrt[3]{\lambda_{PB}})}{d_m/d_{ox}} \tag{7}$$

where, the subscript $_m$ denotes matrix and $_{ox}$ denotes oxide, respectively. λ_{PB} is the Pilling Bedworth Ratio, which is the ratio of the molar volumes of the oxide to the molar volumes of the metal. d_m is the distance between two inner oxides, which approximately equal to the grain size because the internal oxides usually distributed along the grain boundaries. d_{ox} is the width of the internal oxide.

(ii) Due to the mismatch of CTEs between the internal oxides and

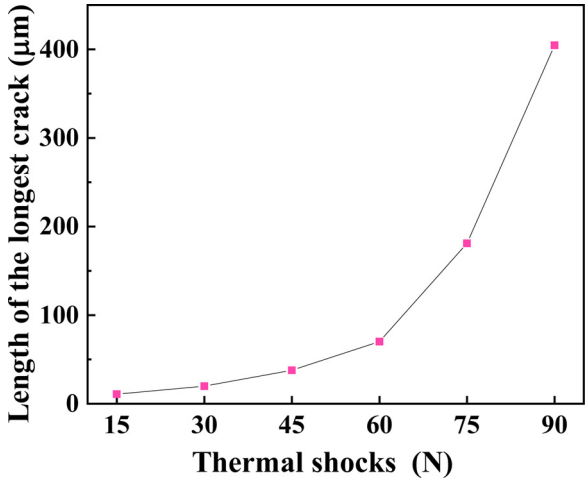

Fig. 10. The relationship between the longest crack length and thermal-shock cycles.

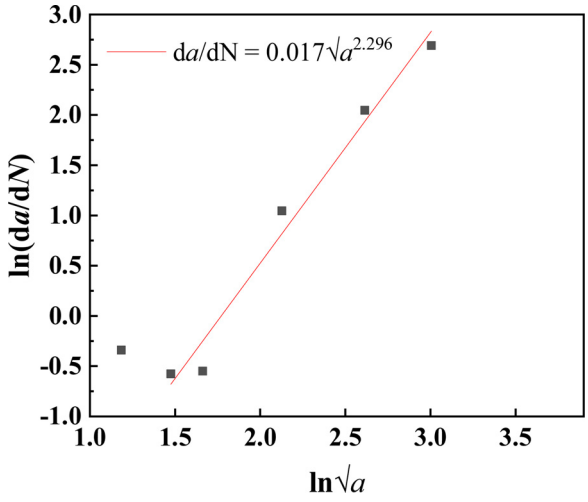

Fig. 11. The linear fitting curve between the crack growth rate and the crack length.

the matrix, residual compressive stress during heating and tensile stress during cooling can be expected in oxides. We assume that the elastic modulus, μ, and α is not changed with temperature, the thermal stress caused by the mismatch of CTEs during cooling process can be calculated with Eqs. (8) and (9) [42].

$$\sigma_{ox} = \frac{E_{ox}}{1-\mu_{ox}} \frac{(\alpha_m - \alpha_{ox})}{1 + \frac{d_{ox}}{d_m}\frac{E_{ox}}{E_m}\frac{(1-\mu_m)}{(1-\mu_{ox})}} \Delta T \tag{8}$$

$$\sigma_m = \frac{E_m}{1-\mu_m} \frac{(\alpha_{ox} - \alpha_m)}{1 + \frac{d_m}{d_{ox}}\frac{E_m}{E_{ox}}\frac{(1-\mu_{ox})}{(1-\mu_m)}} \Delta T \tag{9}$$

Table 1
Physical parameters of Cr_2O_3, Co, and the present alloy.

System	Thermal expansion coefficient $\alpha/(10^{-6}/K)$	Elastic modulus E/(GPa)	Poisson's ratio μ
Cr_2O_3	9.6 [37]	286 [38]	0.27 [39]
Co	13 [40]	209 [40]	0.51 [41]
Present alloy[a]	11.013	207	0.3

[a] Experimental.

(iii) The temperature gradient exists at the oxide/matrix interface due to the inadequate quality of poor heat transfer between the oxide and the matrix. The so-induced stress can be calculated by Eq. (6).

Here, we choose Cr_2O_3 as the represent oxide and Fig. 8(d) as the represent distribution picture of internal oxides. The width of the internal oxides is measured as about 0.2 μm by the ImageJ software. Combined by the above parameters provided in Table 1, the stresses induced in the thermal-shock process are listed in Table 2. The stress caused by the volume change of internal oxides is about -3.34 GPa. The stress induced by the mismatch of CTEs during cooling is about 1.01 GPa in the internal oxides and 0.03 GPa in the matrix. Stress induced by the temperature gradient in the oxide is about -2.93 GPa. These stresses are of the same order of magnitude as those previous research [43–45], which reported the stresses in the oxide scale was about -0.4 ~ 3.9 GPa. The actual stress in the oxide and the oxide scale is not an summation of the stresses listed in Table 2, and is smaller than the summation of the stresses listed in Table 2 . It is probably due to the stress relaxation mechanism [42], e.g. the creep of the matrix, creep of oxide, and fracture of oxide.

Anyhow, the internal oxides at the interfaces among the carbide particles and the Co matrix are porous, loose, and brittle [16]. They can weak the coherence between the internal oxides and matrix, which is called oxidation embrittlement. The oxidation during the thermal shocks shortens the incubation time of cracks and reduces the resistance of cracking. With the increase of thermal-shock cycles, the micro-cracks associated with the internal oxides are initiated around the Cr_7C_3 particles and penetrate deep into the specimens with the increased thermal-shock cycles, which are evidenced by the increasing length of

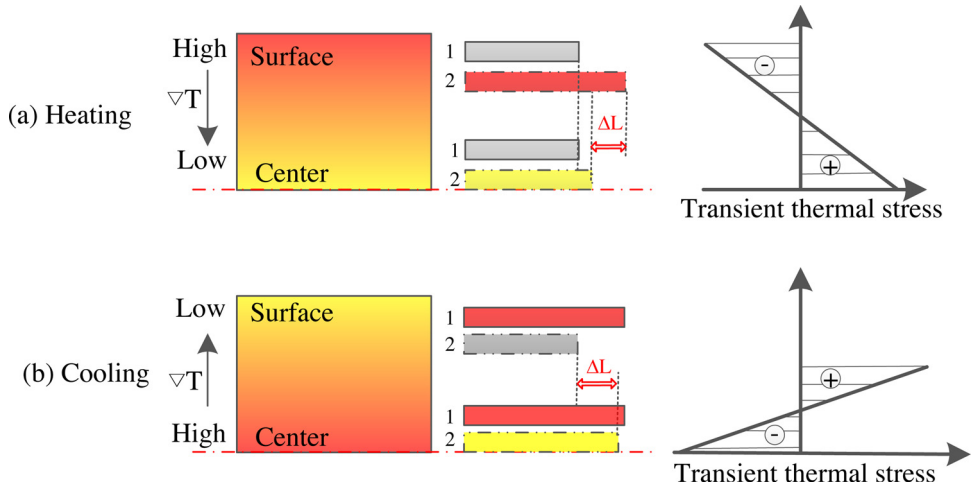

Fig. 12. The transient thermal stress induced at the moment of heating and cooling.

Table 2
Stresses induced by PBR, CTE, and temperature gradient in the oxides, matrix, and the present alloy.

System	Equation	Location	Stress (GPa)	Complement Parameter	Stress in the oxide scale in references
Volume change	$\sigma_m = \frac{E_m}{1-\mu_m}\frac{(1-\sqrt[3]{\lambda_{PB}})}{d_m/d_{ox}}$	Matrix	−3.34	λ_{PB} = 2.07 [27] (Cr_2O_3/Cr)	−3.080 ± 0.88 GPa [43]. −0.4 GPa [44]
CTE mismatch	$\sigma_{ox} = \frac{E_{ox}}{1-\mu_{ox}}\frac{(\alpha_m-\alpha_{ox})}{1+\frac{d_{ox}}{d_m}\frac{E_{ox}}{E_m}\frac{(1-\mu_m)}{(1-\mu_{ox})}}\Delta T$	Internal oxide	1.01	d_m = 7 μm d_{ox} = 0.2 μm △T = 780 °C	−2.6 GPa [45]
	$\sigma_m = \frac{E_m}{1-\mu_m}\frac{(\alpha_{ox}-\alpha_m)}{1+\frac{d_m}{d_{ox}}\frac{E_m}{E_{ox}}\frac{(1-\mu_{ox})}{(1-\mu_m)}}\Delta T$	Matrix	−0.03		
Temperature gradient	$\sigma = \frac{E\alpha}{1-\mu}\Delta T$	Internal oxide	2.93		
		Sample surface	2.54		

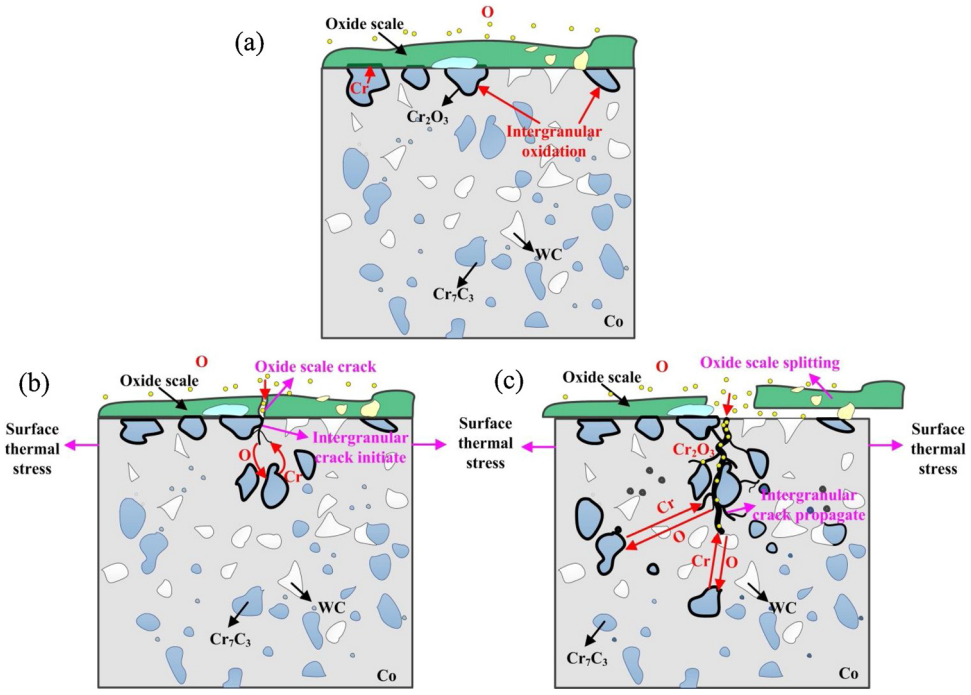

Fig. 13. Schematic of an oxidation-assisted cracking in the thermal-shock process of the Co-based alloy.

cracks in Fig. 8. The thermal stress aroused by the thermal shocks is abrupt and not uniform [8]. The oxides at the crack tip serve as the preferential stress-concentration sites and then accelerate the cracking. After a certain number of thermal-shock cycles, the cracks could be visibly observed and make the specimen fracture.

These giant cracks serve as oxygen diffusion channels, shown in Fig. 9. The O elements rapidly diffuse into the metal along these cracks and strengthen the internal oxidation around the Cr_7C_3 particles. The oxides at the crack tip serve as the preferential stress-concentration sites again and then accelerate the cracking. The damage mode ascribed to the oxidation has been proposed by Neu et al. [17,18] and was also observed by many researchers under the thermal-shock cycles conditions [11,15,46] as well as under isothermal fatigue conditions [47].

As a summary of the above analysis, Fig. 13 presents the process of an oxidation-assisted and oxidation-accelerated cracking during thermal shock process. After a short time of oxidation, a thin oxide scale is produced on the specimen, and the internal oxidation occurs beneath the oxide scale, as presented in Fig. 13(a). The crack is easy to be produced at the oxide scale during the thermal shock process because thermophysical properties of the oxides and the matrix have significant differences. The oxide scale is susceptible to peeling off with the increase of the thermal-shock cycles, as illustrated in Figs. 13(b) and (c). Without the protective oxide scale, the internal oxidation is disastrous. The pocket-like internal oxides in Figs. 5, 8, and 9(a) serve as the preferential stress-concentration sites. The internal oxides become the crack initiation sites and accelerate the crack propagation during the thermal-shock process.

What's more, oxidation during the thermal shocks is thermal stress-assisted and cracking-accelerated. The generated stress arising from the concomitant oxidation-diffusion-creep processes [26] during the heating treatment makes the oxides grow and preferentially penetrate the substrate. The tension stress accelerates the diffusion coefficient of O and Cr elements [48] and leads the grain boundaries to be covered with more oxides than the matrix [20,21,49]. When the rapid diffuse O elements channels associated with the cracks are generated into the substrate, as illustrated in Figs. 13(b) and (c), the oxidation rate is accelerated.

5. Conclusion

The internal oxidation and cracking behavior of a new Co-based alloy were observed and analyzed during the thermal shocks at temperatures of 800 °C - RT and in static oxidation at 800 °C.

(1) The interfaces between the Cr_7C_3 particles and the Co matrix are preferentially oxidized during the thermal shocks. The internal oxides with the pocket-like feature are produced around the Cr_7C_3 particles.

(2) The oxidation during thermal shocks is much more disastrous than that during static oxidation. The oxidation during the thermal shocks is accelerated by the thermal stress and cracks generated during thermal shocks.

(3) The crack growth rate of this new Co-based alloy during the thermal shocks obeys Paris's law and is dominated by the thermal stress, and accelerated by oxidation.

Data availability

The raw/processed data required to reproduce these findings cannot be shared at this time as the data also forms part of an ongoing study.

CRediT authorship contribution statement

Junxia Wen: Data curation, Investigation, Methodology, Visualization, Writing - original draft, Writing - review & editing. **Rui Cao:** Conceptualization, Funding acquisition, Writing - review & editing. **Hongyan Che:** Resources. **Hao Dong:** Resources. **Haiyan Zhang:** Data curation, Investigation, Methodology. **Yingjie Yan:** Writing - review & editing. **Yanfei Gao:** Conceptualization, Funding acquisition, Writing - review & editing. **Peter K Liaw:** Conceptualization, Funding acquisition, Writing - review & editing.

Declaration of Competing Interest

The authors declare that they have no known competing financial interests or personal relationships that could have appeared to influence the work reported in this paper.

Acknowledgments

This investigation was supported by the National Nature Science Foundation of China (Nos. 51761027, 51675255). J.X. Wen very much thanks to the support from the excellent students studying abroad foundation of Lanzhou University of Technology. PKL very much appreciates the support of the National Science Foundation (DMR-1611180 and 1809640) with the program directors, Drs. G. Shiflet and D. Farkas.

Appendix A. Supplementary data

Supplementary material related to this article can be found, in the online version, at doi:https://doi.org/10.1016/j.corsci.2020.108828.

References

[1] R. Liu, J. Yao, Q. Zhang, M.X. Yao, R. Collier, Effects of molybdenum content on the wear/erosion and corrosion performance of low-carbon Stellite alloys, Mater. Design 78 (2015) 95–106, https://doi.org/10.1016/j.matdes.2015.04.030.
[2] J.-N. Aoh, J.-C. Chen, On the wear characteristics of cobalt-based hardfacing layer after thermal fatigue and oxidation, Wear 250 (2001) 611–620, https://doi.org/10.1016/S0043-1648(01)00668-8.
[3] M.X. Yao, J.B.C. Wu, Y. Xie, Wear, corrosion and cracking resistance of some W- or Mo-containing Stellite hardfacing alloys, Mater. Sci. Eng. A 407 (2005) 234–244, https://doi.org/10.1016/j.msea.2005.06.062.
[4] S. Lee, Y. Lu, P. Liaw, L. Chen, S. Thompson, J. Blust, P. Browning, A. Bhattacharya, J. Aurrecoechea, D. Klarstrom, Hold-time effects on elevated-temperature low-cycle-fatigue and crack-propagation behaviors of HAYNES® 188 superalloy, J. Mater. Sci. 44 (2009) 2945–2956, https://doi.org/10.1007/s10853-009-3391-1.
[5] L. Jiang, H. Wang, P.K. Liaw, C.R. Brooks, D.L. Klarstrom, Temperature evolution during low-cycle fatigue of ULTIMET® alloy: experiment and modeling, Mechanics Mater. 36 (2004) 73–84, https://doi.org/10.1016/S0167-6636(03)00032-2.
[6] R. Cao, H.Y. Zhang, G.H. Liu, H.Y. Che, J.H. Chen, Effect of thermal cycle shocking on microstructure and mechanical properties of Stellite 12 (Co-29Cr-2.3C-3W) cobalt based alloy, Mater. Sci. Eng. A 714 (2018) 68–74, https://doi.org/10.1016/j.msea.2017.12.057.
[7] J.H. Perepezko, The hotter the engine, the better, Science 326 (2009) 1068–1069, https://doi.org/10.1126/science.1179327.
[8] D. Li, W. Li, R. Wang, H. Kou, Influence of thermal shock damage on the flexure strength of alumina ceramic at different temperatures, Mater. Lett. 173 (2016) 91–94, https://doi.org/10.1016/j.matlet.2016.03.026.
[9] W.D. Kingery, Factors affecting thermal stress resistance of ceramic materials, J. Am. Ceram. Soc. 38 (1955) 3–15, https://doi.org/10.1111/j.1151-2916.1955.tb14545.x.
[10] H. Xinping, Z. Guoqun, W. Bingyao, Temperature change and stress distribution analysis of die surface in Al-alloy die casting process and experimental study on die heat check, Res. Develop. (2008) CNKI:SUN:ZZAF.0.2008-01-013CNKI:SUN:ZZAF.0.2008-01-013 https://doi.org/CNKI:SUN:ZZAF.0.2008-01-013.
[11] D. Matisková, Š. Gašpar, L. Mura, Thermal factors of die casting and their impact on the service life of moulds and the quality of castings, Acta. Polytechnica Hungarica 10 (2013) 65–78, https://doi.org/10.12700/APH.10.03.2013.3.6.
[12] S. Suresh, Fatigue of materials, Cambridge university press, 1998.
[13] C.A. Barrett, C.E. Lowell, The cyclic oxidation resistance of cobalt-chromium-aluminum alloys at 1100 and 1200° C and a comparison with the nickel-chromium-aluminum alloy system, Oxidation Metals 12 (1978) 293–311, https://doi.org/10.1007/BF00603574.
[14] P. Tunthawiroon, Y. Li, Y. Koizumi, A. Chiba, Strain-controlled iso-thermal fatigue behavior of Co–29Cr–6Mo used for tooling materials in Al die casting, Mater. Sci. Eng. A 703 (2017) 27–36, https://doi.org/10.1016/j.msea.2017.07.047.
[15] F. Yang, X. Sun, H. Guan, Z. Hu, High-temperature low-cycle fatigue behavior of K40S cobalt-base superalloy, Metallurgical Mater. Transact. A 34 (2003) 979–986, https://doi.org/10.1007/s11661-003-0227-5.
[16] Z. Azari, M. Abbadi, H. Moustabchir, M. Lebienvenu, The influence of fatigue cycling on the oxidation kinetics and crack initiation of a Cr–Mo steel, Int. J. Fatigue 30 (2008) 517–527, https://doi.org/10.1016/j.ijfatigue.2007.03.011.
[17] R. Neu, H. Sehitoglu, Thermomechanical fatigue, oxidation, and creep: Part I. Damage mechanisms, Metallurgical Transact. A 20 (1989) 1755–1767, https://doi.org/10.1007/BF02663207.
[18] R. Neu, H. Sehitoglu, Thermomechanical fatigue, oxidation, and creep: Part II. Life prediction, Metallurgical Transact. A 20 (1989) 1769–1783, https://doi.org/10.1007/BF02663208.
[19] M. Valsan, D. Sastry, K.B. Sankara Rao, S. Mannan, Effect of strain rate on the high-temperature low-cycle fatigue properties of a nimonic PE-16 superalloy, Metallurgical Mater. Transact. A 25 (1994) 159–171, https://doi.org/10.1007/bf02646684.
[20] M. Lafata, L. Rettberg, M. He, T. Pollock, Oxidation-assisted crack growth in single-crystal superalloys during fatigue with compressive holds, Metallurgical Mater. Transact. A 49 (2018) 105–116, https://doi.org/10.1007/s11661-017-4392-3.
[21] L. Viskari, M. Hörnqvist, K. Moore, Y. Cao, K. Stiller, Intergranular crack tip oxidation in a Ni-base superalloy, Acta. Mater. 61 (2013) 3630–3639, https://doi.org/10.1016/j.actamat.2013.02.050.
[22] F.H. Stott, The protective action of oxide scales in gaseous environments at high temperature, Reports Progress Phys. 50 (1987) 861–913, https://doi.org/10.1088/0034-4885/50/7/002.
[23] A. Atkinson, Transport processes during the growth of oxide films at elevated temperature, Reviews Modern Physics 57 (1985) 437 https://doi.org/0.1103/RevModPhys.57.437.
[24] J.-Y. Yen, J.-G. Hwu, Stress effect on the kinetics of silicon thermal oxidation, J. Appl. Phys. 89 (2001) 3027–3032, https://doi.org/10.1063/1.1342801.
[25] T. Shoji, K. Sakaguchi, Z. Lu, S. Hirano, Y. Hasegawa, T.-a. Kobayashi, K. Fujimoto, Y. Nomura, Effects of cold work and stress on oxidation and SCC behavior of stainless steels in PWR primary water environments, Revue Générale Nucléaire (2011) 50–62, https://doi.org/10.1051/rgn/20111050.
[26] J. Wen, R. Cao, Y. Gao, Mysterious Failure in Load-Free Superalloys under Repeated Thermal Shocks, Acta. Mater. 194 (2020) 276–282, https://doi.org/10.1016/j.actamat.2020.05.002.
[27] J. Wen, H. Che, R. Cao, H. Dong, Y. Ye, H. Zhang, J. Brechtl, Y. Gao, P.K. Liaw, Evolution of the mechanical properties of a cobalt-based alloy under thermal shocks, Mater. Design 188 (2020) 108425, , https://doi.org/10.1016/j.matdes.2019.108425.
[28] G. Antipas, Review of gas atomisation and spray forming phenomenology, Powder Metallurgy 56 (2013) 317–330, https://doi.org/10.1179/1743290113Y.0000000057.
[29] N.S. Neelam, B. S, A. Bhattacharjee, N.R. Gvs, M.A. Zafir, Comparison of the isothermal and cyclic oxidation behavior of Cr and Mo containing γ-TiAlNb alloys, Corr. Sci. 163 (2020) 108300, , https://doi.org/10.1016/j.corsci.2019.108300.
[30] S. Anthonysamy, K. Ananthasivan, I. Kaliappan, V. Chandramouli, P.R. Vasudeva Rao, C.K. Mathews, K.T. Jacob, Gibbs energies of formation of chromium carbides, Metallurgical Mater. Transact. A 27 (1996) 1919–1924, https://doi.org/10.1007/bf02651941.
[31] W.-M. Gui, H.-Y. Zhang, M. Yang, T. Jin, X.-F. Sun, Q. Zheng, The Intrinsic Relationship Between Microstructure Evolution and Thermal Fatigue Behavior of a Single-Crystal Cobalt-Base Superalloy, Acta. Metallurgica Sinica (English Letters) 30 (2017) 1192–1200, https://doi.org/10.1007/s40195-017-0646-8.
[32] S.-R.A, R. Turrubiates-Estrada, H.F. Lopez, FCC to HCP transformation kinetics in a Co–27Cr–5Mo–0.23C alloy, J. Mater. ence 46 (2011) 254–262, https://doi.org/10.1007/s10853-010-4969-3.
[33] R.A. RAPP, Kinetics, microstructures and mechanism of internal oxidation-its effect and prevention in high temperature alloy oxidation, Corrosion 21 (1965) 382–401, https://doi.org/10.5006/0010-9312-21.12.382.
[34] P. Paris, F. Erdogan, A critical analysis of crack propagation laws, J. Basic Eng. 85 (1963) 528–533, https://doi.org/10.1115/1.3656900.
[35] R.J. Donahue, H.M. Clark, P. Atanmo, R. Kumble, A.J. McEvily, Crack opening displacement and the rate of fatigue crack growth, Int. J. Fracture Mechanics 8 (1972) 209–219, https://doi.org/10.1007/BF00703882.
[36] D. Duquette, H. Uhlig, Critical reaction rate for corrosion fatigue of 0.18% carbon steel and the effect of PH, ASM Trans Quart 62 (1969) 839–845.
[37] W. Martienssen, H. Warlimont, Handbook of Condensed Matter and Materials Data, Springer, 2005.
[38] I. Saeki, T. Ohno, D. Seto, O. Sakai, Y. Sugiyama, T. Sato, A. Yamauchi,

K. Kurokawa, M. Takeda, T. Onishi, Measurement of Young's modulus of oxides at high temperature related to the oxidation study, Mater. High Temperatures 28 (2014) 264–268, https://doi.org/10.3184/096034011x13182685579795.
[39] https://materialsproject.org/materials/mp-19399/#elastic-tensor. https://doi.org/10.17188/1194409.
[40] https://periodictable.com/Elements/027/data.wt.html.
[41] https://materialsproject.org/materials/mp-669382/#elastic-tensor. https://doi.org/10.17188/1281604.
[42] A.M. Huntz, Stresses in NiO, Cr2O3 and Al2O3 oxide scales, Mater. Sci. Eng. A 201 (1995), https://doi.org/10.1016/0921-5093(94)09747-X.
[43] G. Calvarin, A.M. Huntz, A.H.L. Goff, S. Joiret, M.C. Bernard, Oxide Scale Stress Determination by Raman Spectroscopy Application to the NiCr/Cr2O3 System and Influence of Yttrium, Scripta Materialia 38 (1998) 1649–1658, https://doi.org/10.1016/S1359-6462(98)00079-7.
[44] O. Bernard, G. Amiri, C. Haut, B. Feltz, A.M. Huntz, M. Andrieux, Mechanical and microstructural characterisation of oxide films damage, Mater. Sci. Eng. A 335 (2002) 32–42, https://doi.org/10.1016/S0921-5093(01)01931-1.
[45] H. Zhou, J. Qu, M. Cherkaoui, Stress–oxidation interaction in selective oxidation of Cr–Fe alloys, Mechanics Mater. 42 (2010) 63–71, https://doi.org/10.1016/j.mechmat.2009.09.007.
[46] N. Tang, Y. Li, P. Tunthawiroon, Y. Koizumi, A. Chiba, Thermo-mechanical fatigue test of a wrought Co-based alloy as potential tooling material for die casting, Mater. Sci. Eng. A 615 (2014) 164–168, https://doi.org/10.1016/j.msea.2014.07.073.
[47] Q.-C. Jiang, X.-M. Zhao, F. Qiu, T.-N. Ma, Q.-L. Zhao, The Relationship Between Oxidation and Thermal Fatigue of Martensitic Hot-Work Die Steels, Acta. Metallurgica Sinica (English Letters) 31 (2018) 692–698, https://doi.org/10.1007/s40195-017-0699-8.
[48] C. Pu, Y. Gao, Y. Wang, T.-L. Sham, Diffusion-coupled cohesive interface simulations of stress corrosion intergranular cracking in polycrystalline materials, Acta. Mater. 136 (2017) 21–31, https://doi.org/10.1016/j.actamat.2017.06.058.
[49] J. Ramsay, H. Evans, D. Child, M. Taylor, M. Hardy, The influence of stress on the oxidation of a Ni-based superalloy, Corr. Sci. 154 (2019) 277–285, https://doi.org/10.1016/j.corsci.2019.04.023.